Adhikari, Prajesh; Jani, Pallav K.; Hsiao, Lilian C.; Rojas, Orlando J.; Khan, Saad A.

Interfacial Contributions in Nanodiamond-Reinforced Polymeric Fibers

Published in:
Journal of Physical Chemistry B

DOI:
10.1021/acs.jpcb.1c03361

Published: 16/09/2021

Document Version
Peer-reviewed accepted author manuscript, also known as Final accepted manuscript or Post-print

Please cite the original version:
Adhikari, P., Jani, P. K., Hsiao, L. C., Rojas, O. J., & Khan, S. A. (2021). Interfacial Contributions in Nanodiamond-Reinforced Polymeric Fibers. *Journal of Physical Chemistry B*, *125*(36), 10312–10323. https://doi.org/10.1021/acs.jpcb.1c03361

Interfacial Contributions in Nanodiamond-Reinforced Polymeric Fibers

Prajesh Adhikari[1#], *Pallav K. Jani*[1#], *Lilian C. Hsiao*[1], *Orlando J. Rojas*[1,2,3], *and Saad A. Khan*[1,*]

[1]Department of Chemical and Biomolecular Engineering, North Carolina State University,
Raleigh, NC 27695, United States

[3]Biopducts Institute, Departments of Chemical & Biological Engineering, Chemistry, and Wood
Science, The University of British Columbia, Vancouver, BC V6T 1Z3, Canada

[4]Department of Bioproducts and Biosystems, School of Chemical Engineering, Aalto University,
FI-00076 Aalto, Espoo, Finland

(*) Author for Correspondence: Saad A. Khan, Email: khan@eos.ncsu.edu

(#) co-first authors

ABSTRACT

We study the interfacial energy parameters that explain the reinforcement of polymers with nanodiamond (ND) and the development of mechanical strength of ND-reinforced composites. Thermodynamic parameters associated with the surface energy, wettability ratio and work of spreading and dispersion/aggregation transition were used to derive a criterion to predict the dispersibility of carboxylated ND (cND) in polymeric matrices. Such criterion for dispersion (Dc) was applied to cND co-spinning with poly(vinyl alcohol) (PVA), polyacrylonitrile (PAN) and polystyrene (PS). The shift in glass transition temperature (ΔT_g), used as a measure of polymer-cND interactions, revealed a direct correlation with D_c in the order of PAN<PS<PVA, regardless of the amorphous or semi-crystalline nature of the polymer. Contrary to expectation, the tensile strength of the electrospun fibers correlated with the D_c and ΔT_g for semi-crystalline polymers (PVA and PAN) while the amorphous PS displayed a maximum reinforcement with cND. Such conflicting results revealed a synergy that is not captured by thermodynamic considerations but factor the contributions of polymer-cND morphology and stress transfer efficiency. Our findings open the possibility for tailoring the interfacial interactions in polymer-ND composites to achieve maximum mechanical reinforcement.

1. INTRODUCTION

Since their discovery in the 1960s, and the interest gained in the early 2000s,[1] nanodiamonds (NDs) have re-emerged as a carbon-based nanomaterial with potential wide-ranging applications for bioimaging,[2-5] drug delivery,[6-11] electrochemistry,[12-15] tribology.[16-19] as well as coatings and polymer composites.[20-23] Large-scale and low-cost production of commercial NDs is accomplished by detonation synthesis using carbon-containing explosives with a negative oxygen.[24] The resulting product of detonation consists of particles with a diamond core containing graphitic carbon and soot that is further purified via an acid-based treatment. The later oxidizes the non-diamond or graphitic carbon, resulting in ultrafine particles containing carbon-oxygen functionality in the outer periphery.[25-29] Detonation synthesis produces NDs with particle size of roughly 4-10 nm with narrow size distribution, spherical surface morphology, and strong agglomeration potential, in sharp contrast to methods employing high-pressure and high-temperature, which yield larger and inhomogeneous NDs (< 100 nm with broad size distribution) with facetted morphology and low agglomeration potential.[30-31]

After decades of research dedicated toward synthesis, purification, and isolation of NDs, researchers have employed them in numerous applications. Emerging studies pointing towards biocompatibility and low cytotoxicity, in addition to their small particle size and considerable dispersibility in water, have spurred use of NDs for controlled drug release and as a viable alternative to other carbon-based materials with known toxicity.[6,7,32] High mechanical strength coupled with demonstrated anti-corrosion and anti-wear properties have enabled the use of NDs as additives for motor oil lubricants[18] and as low friction coatings in artificial joints.[17] More recently, the ability to tailor the surface functionality of NDs[33] and operate at interphases has instigated research for uses as reinforcing agents in polymer composites[20,22,23] and also as interphase stabilizers. Farias *et al.* harnessed this ability to develop Pickering emulsions with hydroxylated NDs as potential biocompatible Pickering stabilizers.[34]

Despite the useful properties of NDs, they are composed of core aggregates consisting of bridging interparticle bonds that are very difficult to disintegrate. For applications requiring well-controlled particle size, such as in the fabrication of composites using NDs as reinforcing agents, such aggregates may pose significant difficulties during processing. To overcome this challenge, researchers have reported different strategies using heat treatment and oxidation of the confined graphitic layers,[35,36] ultrasound and high-pressure pulse,[37] bead-assisted milling techniques using ceramic, zirconia or silica-based beads as milling agents.[30,31,38-40] Most recently, the development of particle size reduction without contamination using a salt-assisted ultrasonic de-aggregation protocol has opened up opportunities for applications that require nanoparticle size such as in the fabrication of ND-based polymer composites.[41] Several implementations of ND-based polymer composites of polyvinyl alcohol (PVA),[42–45] polymethyl methacrylate (PMMA),[46] poly (L-lactic) acid (PLLA),[47] polyacrylonitrile (PAN),[48] polyethylene (PE)[49] and epoxy resin[50] using solution casting, in-situ polymerization, melt compounding, compression molding, and electrospinning have reported remarkable improvement in material properties such as thermal and electrical conductivity, elastic modulus, tensile strength, elongation at break, toughness, hardness and glass transition temperature. The reader is directed to a recent review of various polymer-ND composite systems.[51]

Although a large number of studies on ND-based polymer composites have successfully demonstrated their reinforcing potential, correlations between the bulk mechanical properties, such as tensile strength, and interfacial interactions between polymer and NDs are still limited. Recent investigations by Wang *et al*., who employed molecular dynamics and semi-empirical quantum chemistry simulations to clarify the effects of nano-pinning of aminated NDs and stretching in reinforcing behavior of epoxy composites, emphasize the need to better understand the polymer-

ND interface.[52] Central to the need for understanding the interfacial energetics of ND-based composites is the unknown effect of the NDs source and purification steps, resulting in subtle variations in particle size and functionality, which manifests into different extent of reinforcing, even within the same polymer matrix under identical processing conditions. Realizing that fundamental understanding of interfacial energy parameters of commercial NDs can aid in the development of a standardized method and allow successful design of ND-based composites, we present an approach that relies on the surface energy of the polymer and ND to understand the role of interfacial energy parameters on polymer/ND interactions, measured using shifts in glass transition temperature (T_g) and the final tensile properties. Using different semi- crystalline and amorphous host polymers with varying polarities – PVA, PAN and polystyrene (PS) - we examine the role of wettability, work of spreading and work associated with the aggregation-dispersion transition on polymer/ND interactions and tensile strength of electrospun polymer-ND composite fibers. Fundamental understanding of interfacial energy parameters could provide a critical path forward in the design of successful strategies to create ND-based composites with reinforced properties.

2. EXPERIMENTAL SECTION

Materials

PVA under the trade name of MW 10-98 (molecular weight ~61 kDa, 98% hydrolyzed, Sigma Aldrich), PAN (molecular weight ~150,000 g/mol, Scientific Polymer Products, NY) and PS (typical M_w ~230,000 and M_n ~140,000, Sigma Aldrich) were used as received. Detonation nanodiamond was produced by Adámas Nanotechnologies, NC and provided in its carboxylated form for a high colloidal stability in water (0.6 wt% ash content, zeta potential -45 mV) and was used without further purification. Dimethylsulfoxide (anhydrous, >99%, Sigma Aldrich), dimethylformamide (anhydrous, 99.8%, Sigma Aldrich), dimethylacetamide (anhydrous, 99.8%, Sigma Aldrich), acetonitrile (anhydrous, 99.8%, Sigma Aldrich), acrylonitrile (>99% contains 35-45 ppm monomethyl ether hydroquinone as inhibitor), acetone (AR, >99.5%, Sigma Aldrich), methanol (anhydrous, 99.8%, Sigma Aldrich), ethanol (99.8%, Sigma Aldrich), chloroform (anhydrous, >99%, Sigma Aldrich), methylene chloride (for high resolution gas chromatography, Fisher Scientific), 1-methyl-2-pyrrolidinone (99% ACS Reagent, Sigma Aldrich), tetrahydrofuran (minimum 99%, Sigma Aldrich), toluene, hexane (for HPLC >95%, Sigma Aldrich), cyclohexane (anhydrous, 99.5%, Sigma Aldrich), ethyl acetate (Certified ACS, Fisher Scientific), acetic anhydride (99% ACS,), sodium hydroxide (NaOH, 1.0 M, Fluka) and sodium chloride (NaCl) (99+% A.C.S Reagent, Sigma Aldrich) were used as received.

2.1 Nanodiamond Dispersion Stability

As received carboxylated nanodiamond (cND) dispersions (1 wt%) were prepared in 18 different solvents with varying dispersive, polar, and hydrogen-bonding components according to the Hildebrand solubility parameter. The solvents included water, dimethylsulfoxide (DMSO), dimethylformamide (DMF), dimethylacetamide (DMAc) acetonitrile, acrylonitrile, acetone, methanol, ethanol, chloroform, dichloromethane (DCM), N-methyl-2-pyrrolidone (NMP), tetrahydrofuran (THF), toluene, hexane, cyclohexane, ethyl acetate and acetic anhydride (See Table S1 for solvent properties). The dispersions were sonicated for 1 h using an ultrasonic bath (Fisher Scientific, 2.8 L) and visually inspected immediately post sonication and after days 1 and 10 to check the stability of the dispersions and to determine the correct solvent system for polymer-cND composite fiber formation.

2.2 Salt-assisted Ultrasonic De-aggregation (SAUD)

cNDs used for nanocomposite fabrication were obtained using the SAUD technique following procedures reported by Turcheniuk *et al.* with minor modifications.[41] Briefly, cND (0.25 g) was added to NaCl (10 g) followed by deionized water (5 ml) in a scintillation vial. The contents were subjected to ultrasonication under an ice-bath to prevent water evaporation using Branson S-450 digital sonifier (power 400 *W*, amplitude 30% and duty cycle 50%) using 1/8” tapered microtip and flat tip for 100 min. Thereafter, the contents were emptied in centrifuge tubes and washed twice with water (50 ml) and centrifuged at 4000 rpm for 10 min (Centrifuge 5702, Eppendorf). The supernatant was discarded, and cND particles were re-suspended in water and centrifuged a second time at 12000 rpm for 1 h. The supernatant was discarded, and the particles were dried in air for 3 days. Dry de-aggregated cND will be referred to as SAUD cND for characterization.

2.2.1 Dynamic Light Scattering (DLS). Particle size and zeta potential of as received cND and SAUD cND were obtained using a zeta potential analyzer (Zeta2000, Malvern Instruments, US) equipped with a 4 mV He-Ne laser (λ = 433 nm). DLS measurements were carried out on dispersions (0.1 wt% and 1 wt%) loaded onto a dip-cell at room temperature. Dispersions were diluted using 1 mM NaCl solution and the reported zeta potential was determined from an average of five measurements.

2.2.2 Fourier-Transform Infrared Spectroscopy (FTIR). FTIR analyses of surface functional groups on as received cND and SAUD cND were performed using Thermo Nicolet iN10 infrared microscope. Approximately 1 mg of particles was mixed with 300 *mg* potassium bromide (KBr) to form a pellet. The spectra were collected using a 4 cm^{-1} resolution and 64 continuous scans over wavenumber range of 4000-500 cm^{-1}.

2.2.3 X-ray Photoelectron Spectroscopy (XPS). The surface elemental composition of as received cND and SAUD cND was analyzed using XPS. Wide scan spectra were acquired over binding energy range of 0-1100 eV on SPECS FlexMod XPS using Mg kα excitation source (1254 eV) and 10^{-10} mbar base pressure in the analysis chamber. XPSPeak4.1 program was used to calibrate spectrum by referencing to adventitious carbon (C1s line at 285.0 eV) and to determine peak areas and elemental composition.

2.2.4 Conductometric Titration. Surface carboxylic acid content of as received cND and SAUD cND was determined using procedure described elsewhere.[53] Briefly, ND samples (3 wt%) were dispersed in 100 mL water and initial pH was recorded. 0.1 M hydrochloric acid and 10 mM NaCl were added to protonate ND samples. 0.04 M NaOH was used for titration and the volume of NaOH and pH were recorded. Surface carboxylic acid content (mmol/g) was determined using, $n_{-COOH} = \left(C_{NaOH} V_{NaOH}\right) / m_{cND}$ where n_{-COOH} is number of moles of carboxylic acid groups, C_{NaOH} is concentration of NaOH (M), V_{NaOH} is volume of NaOH (mL) and m_{cND} is mass of the ND sample (g). Hereon, any reference to cND refers to SAUD c-ND unless stated otherwise.

2.3 Surface Energy Measurement

The surface energy of cND was estimated using the Owens-Wendt plot,[54] described in detail in the corresponding Results & Discussion section, which requires measurement of the equilibrium contact angle of probe liquids with known polar and dispersive surface energy components on the solid surface. Accurate determination of equilibrium contact angle of liquids on powders and porous materials such as cND can be challenging. Common measurements techniques such as goniometry (sessile drop) and Wilhelmy plate methods[55–58] have been applied in the past by converting porous materials into pellets and films. However, these methods seldomly account for surface roughness, inhomogeneity, liquid penetration in pores and swelling effects. Additional techniques such as gel trapping, inverse gas chromatography, and thin-layer wicking technique using Washburn equation have been used previously for measuring contact angles on submicrometer silica particles, cellulose nanofibrils and commercial nanopowders of silica respectively.[59–64] Among these methods, thin-layer wicking technique based on measuring rates of probe liquid penetration into porous cNDs loaded on a thin vertical column, combined with the Washburn equation (eq 1) was considered suitable to estimate the static contact angle of probe liquids on cNDs.

$$m^2 = \left(\frac{C\rho^2}{\eta} \gamma_L \cos\theta \right) t \qquad (1)$$

Here, m is the mass of the liquid uptake at time t, C is the unknown capillary factor within the powder packing, ρ, η and γ_L are the density, apparent viscosity and total surface energy of the probe liquid respectively and θ is the static contact angle.

Wicking experiments were performed using Dynamic Contact Angle Analyzer (Cahn, US). Approximately 100 mg of cND particles were packed in a glass tubing (i.d. 4.9 mm) with a rigid porous base and left overnight to saturate in the vapor of probe liquid. The geometric factor *C* was obtained through wicking experiments using low surface energy probe liquid, such as hexane, that completely wets the particles ($cos\theta = 1$ in eq 1) and this value was held constant for wicking experiments performed using three different probe liquids – diiodomethane ($\gamma_L^d = 50.8\ mJ/m^2, \gamma_L^p = 0\ mJ/m^2$), DMF ($\gamma_L^d = 25.2\ mJ/m^2, \gamma_L^p = 11.3\ mJ/m^2$) and water ($\gamma_L^d = 21.8\ mJ/m^2, \gamma_L^p = 51\ mJ/m^2$), where γ_L^d and γ_L^p are the dispersive and polar surface energy components of the probe liquid. Increase in weight due to rising liquid was monitored until a stable weight gain was achieved after ~10-15 min. Reported values of surface energies were obtained using an average of five independent measurements.

2.4 Electrospun cND-reinforced Polymer Nanofiber Synthesis

PVA, PAN and PS nanofibers with different cND loadings (0.1, 0.5, 1 and 2 wt%) were fabricated using an electrospinning setup consisting of a stationary collector. Polymer/cND solutions were sonicated for 15 min prior to loading in a syringe with a needle attachment (ϕ = 0.3 mm). The syringe was loaded in a syringe pump (Model No. 2345) that controlled the flow rate between 0.5-1 mL/h. A high voltage supply power (Model No. 1721) was used to impart voltage between 15-25 kV at the needle tip. The fibers were collected on an aluminum foil wrapped on the grounded stationary collector plate placed 10-15 cm away from the needle tip. The experiments were carried out at room temperature (20-25°C) with relative humidity between 20-40%. Fibers were collected and placed in a vacuum oven for 3 h to remove moisture and then placed in a desiccator for storage. Detailed description of electrospinning conditions is provided (Table S2). Effect of cND addition on morphology and thermal stability of nanofiber mats was also evaluated and is detailed in the Supplementary Information.

2.4.1 Glass Transition Temperature (T_g). Differential scanning calorimetry (DSC) (Q2000, TA Instruments, US) experiments were performed on electrospun polymer nanofibers with and without cND to determine their T_g. The temperature was increased form 40°C to 300°C with a heating rate of 10°C/min and then cooled back to 40°C at 10°C/min under nitrogen flow. The reported T_g is the average over three replicates.

2.4.2 Tensile Properties. Dynamic mechanical analyzer (RSA-G2, TA Instruments, US) was utilized to obtain stress-strain curves for nanofiber specimens at room temperature with extension rates between 0.15-0.30 mm/min depending on the polymer. Thick nanofiber mats, cut into rectangular strips (15 x 5 x 0.6-0.7 mm), were loaded with gauge gap of 5 mm. All reported values are average of at least five measurements.

3. RESULTS AND DISCUSSION

3.1 Nanodiamond Dispersion Stability

As received cND dispersed in different solvents were classified as stable (water, DMF, DMAc, NMP, and acetic anhydride), moderately stable (acetone, methanol, and ethanol), less stable (acetonitrile and acrylonitrile) and unstable (DMSO, chloroform, DCM, THF, toluene, hexane, cyclohexane, and ethyl acetate) based on visual differences in the color of the colloidal suspension 10 days post sonication (Figure 1a), with dispersion in water being the most stable. A dispersion map relates the cND dispersion state to the dispersive (δ_d) and polar (δ_p) components of the solvent's Hildebrand solubility parameter (Figure 1b). We found cND dispersions to be unstable until a critical polarity is reached ($\delta_p \,\square\, 7\ MPa^{1/2}$ for solvents used in this study). Dispersion stability appeared to be independent of the dispersive component of the solubility parameter ($\delta_d \,\square\, 14.7-18.4\ MPa^{1/2}$), indicating negligible contributions of the non-polar character of solvents to stabilization of cND. Previous work on the rheology of NDs in mineral oil further corroborates the influence of oil polarity in ND dispersibility.[65] Solvent polarity aids in the dissociation of surface carboxylic acid groups on nanodiamonds into corresponding ions, increasing the conductivity, and further electrostatically stabilizing the system. Despite the polarity, however, the cND dispersion in DMSO was unstable. Dispersion maps relating the hydrogen bonding component (δ_h) of the solubility parameter to the polar and dispersive components reveal no obvious correlations with the state of the dispersion =, strongly indicating the dominant influence of solvent polarity in forming stable cND dispersions (Figure S2).

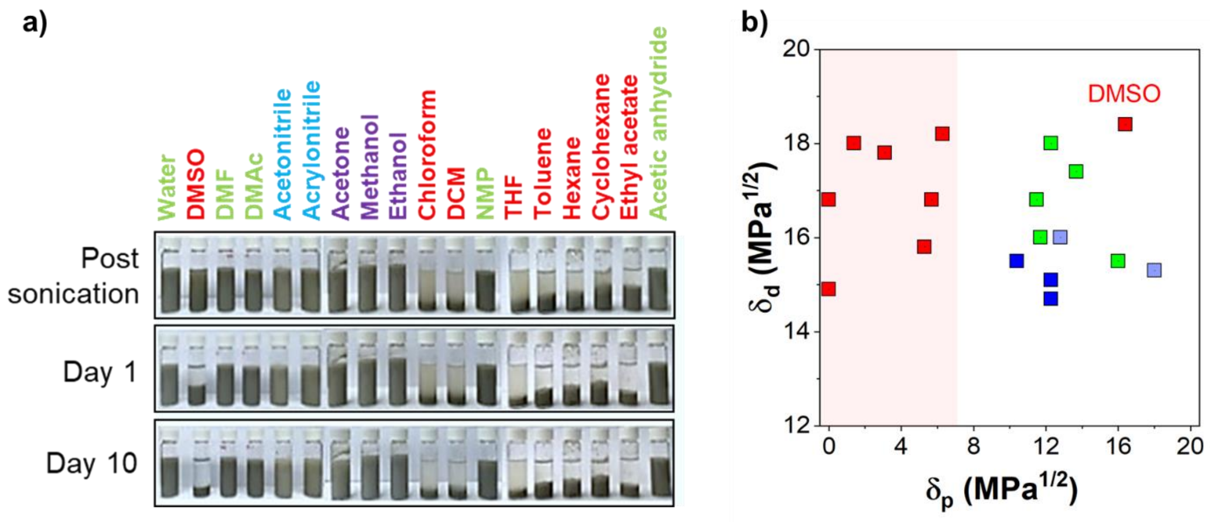

Figure 1. (a) cND dispersions in different solvents imaged immediately post sonication and after days 1 and 10 to visually inspect dispersion stability. (b) Dispersion map illustrating different cND dispersion states – unstable (red), less stable (light blue), moderately stable (blue) and stable (green).

3.2 As Received cND vs SAUD cND

The stability and particle size of as received cND dispersion in water was tested using DLS. The dispersions are opaque and brown, suggesting the presence of particles with sizes capable of scattering light. The cND particles in the dispersions aggregate over time, with visible particle settling at the bottom of the vial; however, the particle size remains unchanged within the sample, suggesting stable dispersion (Figure S3). In contrast to 0.1 wt% cND dispersions (particle size ~90 nm), the 1 wt% cND dispersion resulted in more visible aggregation and higher particle size ~105 nm (Figure S3).

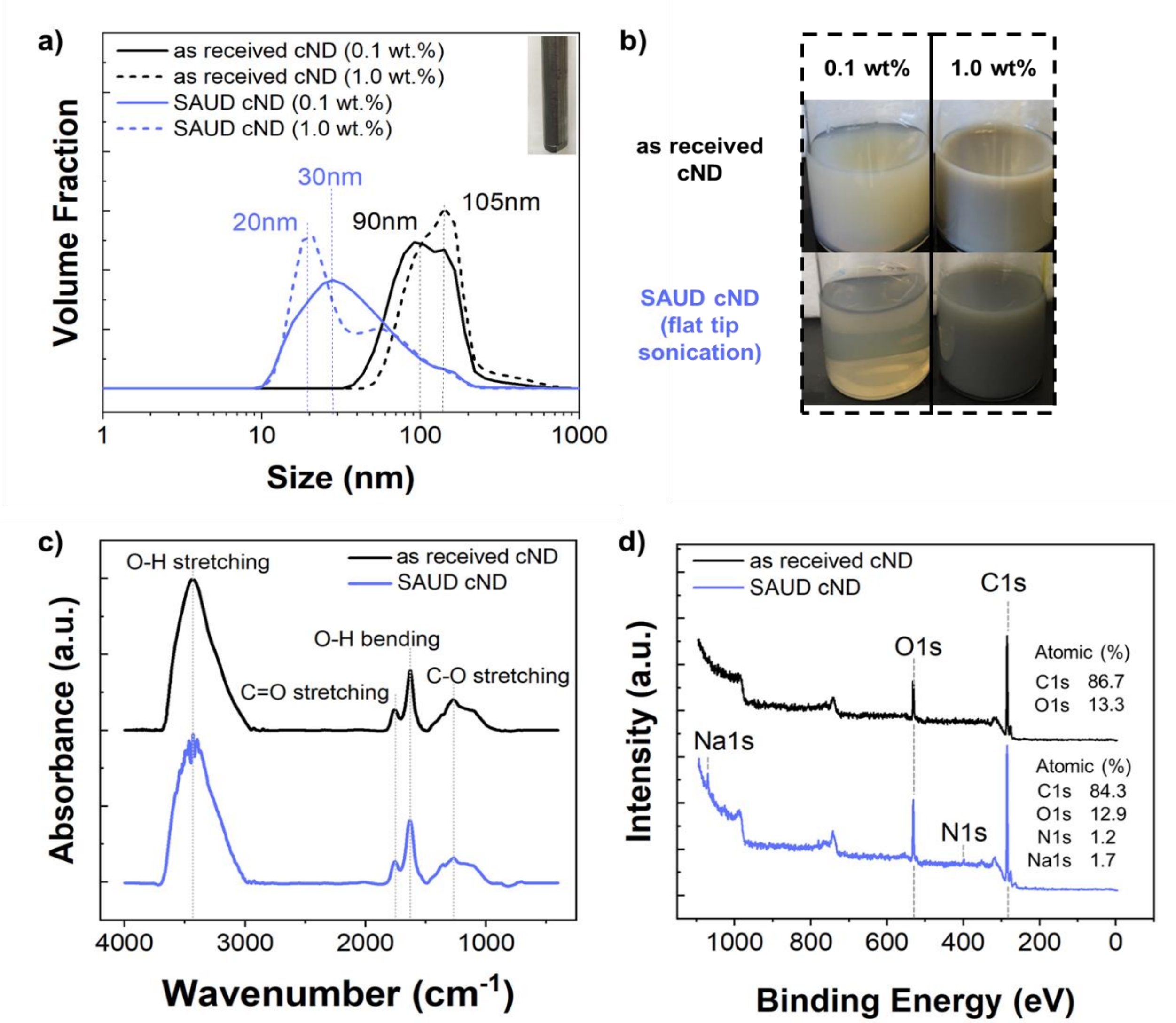

Figure 2. Comparison of cNDs processed through SAUD technique (SAUD cND) and as received cNDs demonstrating (a) reduction in particle size for 0.1wt% and 1.0wt% samples (flat tip sonication) via DLS measurements using refractive index of 1.427 and viscosity of 0.899 mPa.s. (b) Visual differences in cND dispersions after 10 days. Note the insignificant changes in surface functionality through (c) FTIR spectra and (d) XPS survey scans.

Aggregation of nano-sized fillers due to large cohesive forces is an active hindrance to the field of polymer nanocomposites. Indeed, for our polymer/cND fiber composite electrospun fibers with

~100 nm as received cNDs, visible aggregates at 2 wt% loading were observed with no mechanical reinforcement. Hence smaller particle size of as received cND was achieved using the SAUD technique as previously described and the resulting SAUD cNDs were used for electrospinning composite fibers. DLS measurements demonstrate the reduction in particle size of SAUD cNDs compared to the as received cNDs for sonication with both the flat tip (Figure 2a) and the micro tip (Figure S4). The flat tip sonication resulted in a smaller particle size (20-30 nm) compared to that achieved with the micro tip (50 nm) , a consequence of the difference in energy imparted by tips during sonication. FTIR, XPS and conductometric titrations were performed on both the as received cNDs and SAUD cNDs to ascertain any changes in surface functionality. IR spectra for both cND samples demonstrate no significant changes, with both as received cND and SAUD cND showing absorption peaks due to hydroxyl bond stretching between 3700-3000 cm^{-1}, hydroxyl bond bending at 1625 cm^{-1} and carbonyl bond stretching at 1730 cm^{-1} arising from the carboxylic acid groups on the ND surface[66] (Figure 2c). XPS survey scans showed as received cNDs to be predominantly carbon (86.7%), with some oxygen (13.3%) due to the presence of surface acid groups. After de-aggregation, SAUD c-NDs had similar atomic content for carbon (84.3%) and oxygen (12.9%). A trace amount of sodium (~1.7%) due to the presence of salt during the SAUD process and nitrogen (~1.2%) was noted (Figure 2d). Conductometric titrations (Figure S5) revealed the surface carboxylic acid content was approximately 0.06 mmol/g for as received cNDs and 0.05 mmol/g for SAUD cNDs, indicating minor changes in surface functionality. The minor reduction in carboxylic acid content could be due to trace sodium ions interacting with free surface carboxylic acid groups. This was also reflected in zeta potential of as received cNDs (-53.3 mV) and SAUD cNDs (-48.8 mV). Any reference to cND from here on refers to SAUD cND.

3.3 Nanodiamond Surface Energy

In the determination of surface free energy of a solid (in this case cND particles), the experimental inaccessibility of energetics associated with the solid-vapor interface (γ_{SV}) and solid-liquid interface (γ_{SL}) in the classical Young's equation have spurred development of methods to measure them indirectly. A unifying theory for determination of γ_{SV} and γ_{SL} does not exist; however, pioneering work by Zisman[67] and Fowkes,[68] further extended by Owens-Wendt,[54] and van Oss[69] are well-accepted approaches. Such approaches rely on measurements of contact angle on solid surfaces using solvents with different dispersive (γ_L^d) and polar surface energies (γ_L^p). The two most important but competing theoretical models include theory of surface tension components (STC) pioneered by Fowkes[68] and EOS (equation of state) approach based on macroscopic thermodynamics proposed by Neumann.[70-72] While both these approaches require measurement of contact angles on solid surfaces, STC theory relies on resolving γ_{SL} into contributions from dispersive and polar intermolecular forces, making γ_{SL} a function of type and magnitude of intermolecular forces (van der Waal's, hydrogen bonding, electrostatics) operating between interfaces. EOS theory, on the contrary, eliminates the components and identifies γ_{SL} as a function of total surface tension of solid and liquid phases, i.e., $\gamma_{SL} = f(\gamma_{SV}, \gamma_{LV})$. Although Neumann has shown the existence of identical contact angles on the solid surface of liquids with same total liquid surface tension and independent of the magnitude of dispersive components,[72] Graf *et al.* demonstrated the failure of EOS approach in Langmuir wetting configuration.[73] The reader is directed to previous work describing limitations of EOS approach.[74] Therefore, among all the models present in literature, the Owens-Wendt (modified Fowkes) model (eq 2),[54,68] substituted with Good-Girifalco's geometric mean approximation of interfacial energies,[75] which requires equilibrium contact angle of probe liquids, was considered appropriate for this work in the approximation of surface energy of cNDs.

$$\frac{\gamma_L(1+\cos\theta)}{2\sqrt{\gamma_L^d}} = \sqrt{\gamma_{cND}^p}\left(\frac{\sqrt{\gamma_L^p}}{\sqrt{\gamma_L^d}}\right) + \sqrt{\gamma_{cND}^d} \qquad (2)$$

Here, $\gamma_L (= \gamma_L^d + \gamma_L^p)$ is the known total surface energy, γ_L^d and γ_L^p are the dispersive and polar surface energy components respectively of the probe liquids based on STC theory and θ is the equilibrium contact angle between the probe liquid and cND surface to be measured. γ_{cND}^d and γ_{cND}^p are the respective dispersive and polar components of the total cND surface energy (γ_{cND}).

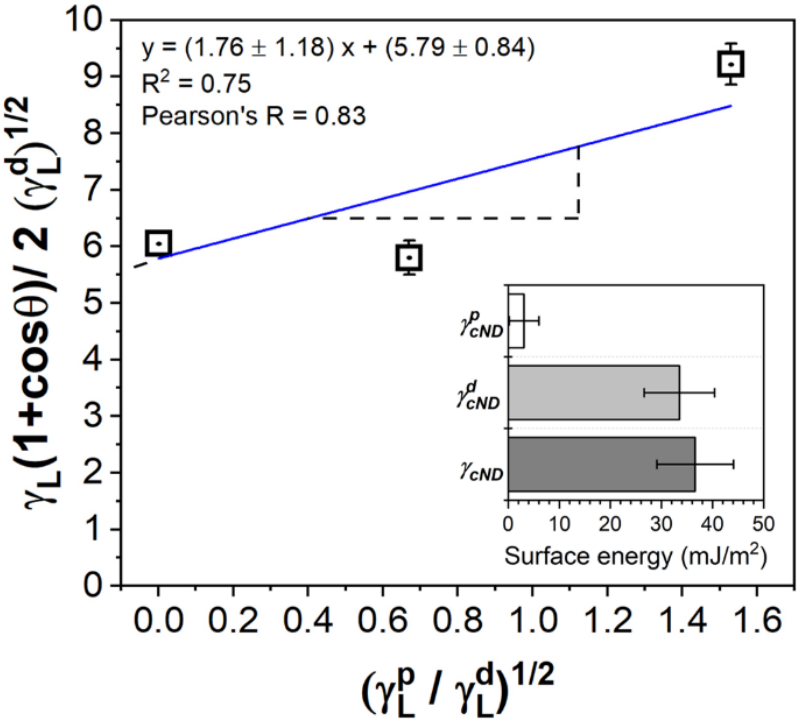

Figure 3. Owens-Wendt plot used to estimate the surface energy components (γ_{cND}^p and γ_{cND}^p) of nanodiamonds using three probe liquids – water, DMF and diiodomethane.

The Owens-Wendt plot (eq 2) resembles a straight line, with the square of the slope and intercept providing an estimate for γ_{cND}^p and γ_{cND}^d. The static contact angles of three probe liquids (water, DMF and diiodomethane) on cND particles were measured by wicking experiments as described earlier. Using the Washburn equation (eq 1), the contact angles on cND were determined to be $77.5° \pm 2.7°$ for water, $62.8° \pm 3.2°$ for DMF and $45.6° \pm 4.3°$ for diiodomethane. Wetting angles determined by eq 1 indicate the slightly hydrophilic character of cND particles. This observation agreed with XPS results (Figure 2d) showing the presence of surface carboxylic groups. Using the Owens-Wendt plot for cND (Figure 3), the total cND surface energy (γ_{cND}) was determined to be $36.6 \pm 7.5\ mJ/m^2$, with a dispersive component of $\gamma_{cND}^{d} = 33.5 \pm 6.9\ mJ/m^2$ and a polar component of $\gamma_{cND}^{p} = 3.1 \pm 2.9\ mJ/m^2$. Errors were likely to stem from deviations in the cND bed packing efficiency inside the glass tube across different experimental runs. It is also worth noting that the surface energy components reported here for cND using the Washburn equation are only apparent values and are expected to differ from those measured with probe liquids on a theoretical flat, homogenous cND film using Young's equation.[76] Nevertheless, these apparent cND surface energies serve as a good starting point to establish a correlation between surface energetics, interfacial interaction, and mechanical properties of polymer-cND composite systems.

3.3.1 Polymer-Nanodiamond Surface Energetics – Theoretical Basis. The relatively low polar component compared to the dispersive component surface energy of cNDs used in this work is expected to significantly influence the overall performance of composites in terms of wetting of cNDs on the polymer, polymer-ND adhesion strength and the driving force for re-aggregation. This influence on polymer-ND interaction can be related to shifts in T_g and final mechanical properties of the resulting electrospun fiber composites. Stockelhuber *et al.* first studied the influence of surface energy of fillers such as carbon black, silica, organoclays and carbon nanotubes, and established thermodynamic predictors such as dispersibility, compatibility, and interfacial adhesion energies, as well as driving force for aggregation of filler, with different rubber polymers.[77] Natarajan *et al.* utilized the preceding work by Stockelhuber *et al.* and proposed a unifying hypothesis relating thermodynamic predictors to shifts in glass transition temperature, a property related to the polymer-filler interface.[78] We utilize these concepts based on surface energy to calculate critical parameters important for ND-based polymer composite fabrication. These parameters include polymer-cND compatibility, wettability, spreading coefficient, and work associated with the dispersion-aggregation transition. Combining these parameters together generates a parameter (D_c), which we use as the criterion for dispersion.

Nanodiamond Compatibility with Polymer (ΔG_{mix} ***).*** The favorable dispersion of cND particles in a polymer is governed by the change in free energy of mixing, which is the difference between the interfacial energy of polymer-cND ($\gamma_{P/cND}$) interface and the initial surface energy of cND (γ_{cND}) (eq 3).

$$\Delta G_{mix} = \gamma_{P/cND} - \gamma_{cND}$$

(3)

To calculate $\gamma_{P/cND}$, we invoke the Young-Dupree equation (eq 4) where $W_{P/cND}$ is the work of adhesion between the wetting species (polymer) and the solid surface (cND).

$$\gamma_{P/cND} = \gamma_P + \gamma_{cND} - W_{P/cND} \tag{4}$$

Combining eqs 3 and 4; and applying the STC theory and the geometric mean approximation of surface energies[75] we get eq 5 - where $\Delta G_{mix} < 0$ implies thermodynamic compatibility of cND with the polymer.

$$\Delta G_{mix} = \gamma_P - W_{P/cND} = \gamma_P - 2\left(\sqrt{\gamma_P^d \gamma_{cND}^d} + \sqrt{\gamma_P^p \gamma_{cND}^p}\right) \tag{5}$$

where, γ_P^d and γ_P^p are the dispersive and polar surface energy components of the polymer.

***Wettability Ratio* ($W_{P/cND}/W_{cND/cND}$) .** A critical parameter required for cNDs to make a good composite is its ability to wet the polymer. Assuming cND is the wetting species on the surface of the polymer, we re-write the Owens-Wendt equation (eq 2) by substituting γ_L as γ_{cND} ;

$$\cos\theta = -1 + 2\frac{\left(\sqrt{\gamma_P^d \gamma_{cND}^d} + \sqrt{\gamma_P^p \gamma_{cND}^p}\right)}{\gamma_{cND}} = -1 + 2\left(\frac{W_{P/cND}}{W_{cND/cND}}\right) \tag{6}$$

Equation 6 demonstrates the effect of polymer-cND interaction (work of adhesion) and cND-cND interaction (work of cohesion) on the wettability of cND with the polymer phase (*cos*θ). A high ratio of the work of adhesion by cohesion would indicate greater wetting ability of cNDs.

***Work of Spreading* (W_S).** Polymer spontaneity to spread on the cND-surface is captured by the work of spreading[78] (eqs 7 and 8). If $W_S > 0$, the polymer phase is expected to spread spontaneously on the cND surface. $W_S \le 0$ indicates partial polymer spreading.

$$W_S = W_{P/cND} - W_{P/P} \tag{7}$$

$$W_S = 2\left(\sqrt{\gamma_P^d \gamma_{cND}^d} + \sqrt{\gamma_P^p \gamma_{cND}^p}\right) - 2\gamma_P \tag{8}$$

***Work Associated with Dispersion-Aggregation Transition* ($\Delta W_{DIS-AGG}$).** To understand how cND aggregation is influenced by the surrounding polymer phase, we define two distinct states of cNDs – well-dispersed and aggregated (Scheme 1). The idealized model assumes cNDs to be quasi-spherical and each sphere denoting a cluster of smaller particles as well as polymers representing spherical blobs.[79] This allows us to define work associated with the dispersion-aggregation transition ($\Delta W_{DIS-AGG}$) as the difference between work of aggregation (W_{AGG}) and work of dispersion (W_{DIS}). Consider the interaction of two cND spheres in the well-dispersed state with each sphere consisting of N units of cND-polymer pair. The work associated with maintaining stable dispersion state is given by eq 9,

$$W_{DIS} = -2N(W_{P/cND}) \tag{9}$$

Scheme 1. Representation of the dispersion-aggregation (left to right) transition model in polymer-cND composite system.

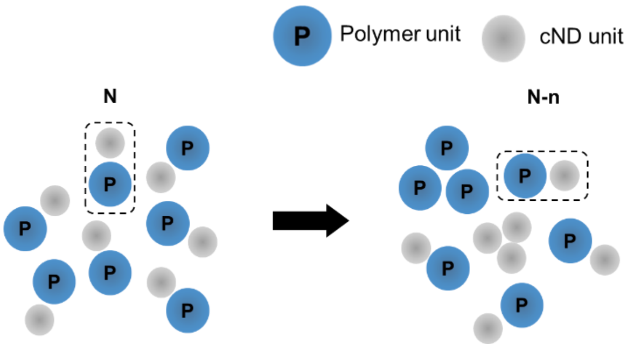

Once the system reaches an aggregated state over time, the two cND spheres approach together and displace n polymer blobs each in the process. The total work associated with this aggregation in terms of adhesive forces at the polymer-cND interface and cohesive forces at the polymer-polymer and cND-cND interfaces is given by eq 10.

$$W_{AGG} = -2\left(N-n\right)W_{P/cND} - n\left(W_{P/P} + W_{cND/cND}\right) \tag{10}$$

The work associated with the dispersion-aggregation transition (eq 11) is then calculated by the difference between eqs 10 and 9.

$$\Delta W_{DIS-AGG} = n\left(W_{P/P} + W_{cND/cND} - 2W_{P/cND}\right) \tag{11}$$

Equation 11 is transformed to its final form (eq 12) by again invoking the Young-Dupree equation, STC theory and Fowkes model discussed earlier. Here, we also simplify the model by assuming n=1.

$$\Delta W_{DIS-AGG} = 2\left(\sqrt{\gamma_P^d} - \sqrt{\gamma_{cND}^d}\right)^2 + 2\left(\sqrt{\gamma_P^p} - \sqrt{\gamma_{cND}^p}\right)^2 \tag{12}$$

Thus, a larger value of $\Delta W_{DIS-AGG}$ represents a larger driving force for cND aggregation.[78]

Criterion for Dispersion of Nanodiamonds in Polymers. In order to develop a correlation between polymer-cND interactions and composite mechanical properties, it is necessary to define a descriptor the encompasses the complex three-way interactions between the polymer-cND, polymer-polymer and cND-cND interfaces. Here, we define a criterion for dispersion (D_c) (eq 13) given as the ratio of the work associated with dispersion-aggregation transition (eq 12) to that associated with polymer spreading on cND surface (eq 8).

$$D_c = \frac{\Delta W_{DIS-AGG}}{W_S} \tag{13}$$

Based on eq 8 and eq 12, it is clear that D_c attempts to encompass all the three interactions ($W_{P/cND}$, $W_{P/P}$ and $W_{cND/cND}$). From eq 12, we find that $\Delta W_{DIS-AGG} > 0$ for all possible polymer-filler combinations (unless surface energies of polymer and cND are identical) and that cNDs will eventually aggregate in the host polymer. For ideal dispersion conditions, the driving force for aggregation ($\Delta W_{DIS-AGG}$) must be minimized and that for polymer spreading on cND (W_S) maximized. This implies that for a polymer-cND combination, D_c must be small and positive to ensure complete dispersion of cNDs in the host polymer. Similarly, a negative D_c implies incomplete dispersion since cohesion forces dominate the polymer-cND adhesion force. Large magnitudes of D_c, irrespective of the sign, indicate poor polymer-cND dispersions state.

3.3.2 Thermodynamic Parameters for cND Dispersion in PVA, PS and PAN. To confirm our hypothesis, we estimate the thermodynamic parameters (ΔG_{mix}, $W_{P/cND} / W_{cND/cND}$, W_S and $\Delta W_{DIS-AGG}$) of cND with two semi-crystalline polymers (PVA and PAN) and amorphous PS. The required surface free energy components (Table 1) of the polymers were obtained from literature[78] and those for cNDs were experimentally determined from the Owens-Wendt plot as previously described (Figure 3).

Table 1. Dispersive and polar components of total surface energy of polymers and cNDs.

Material	γ^d (mJ/m^2)	γ^p (mJ/m^2)	γ (mJ/m^2)
PVA	38.8	5.1	43.9
PS[78]	41.2	0.8	42
PAN	35.0	14.7	49.7
cND (expt.)	33.5 ± 6.9	3.1 ± 2.9	36.6 ± 7.5

Estimated thermodynamic parameters for cND dispersed in the three polymers are plotted (Figure 4a) and tabulated (Table S3). Formation of cND-based polymer composites of all three polymers - PVA, PS and PVA was found to be thermodynamically favored as evident from the negative free energy of mixing, the effect being most pronounced for PVA and least for PAN. The wettability ratio ($W_{P/cND} / W_{cND/cND}$) obtained for the three polymer-cND systems exceeded 1 (Figure 4a) as a consequence of the higher adhesion energy between cND-polymer ($\mathrm{PVA} - 80.1\ mJ/m^2$, $\mathrm{PS} - 77.5\ mJ/m^2$ and $\mathrm{PAN} - 81.9\ mJ/m^2$) than the cohesion energy between nanodiamonds ($73.2\ mJ/m^2$). Note that wettability ratio greater than 1 implies $cos\theta$ greater than 1 (eq 6), which is not physically realizable, but nonetheless, suggested a fully wetted surface and θ of 0°. This indicated that cNDs wet the surface of all polymers. Once cNDs wet the polymer surface, polymers ideally have to spontaneously spread across the cND surface if polymer-cND interactions dominate ($W_S > 0$). The work of spreading was negative for all polymer-cND combinations with the ability of polymers to spread on the cND surface increasing in the order of PAN < PVA < PS (Figure 4a). This suggests that wetting of the cND surface by the polymer is an unfavorable process, a direct consequence of the mismatch in surface energies. Therefore, initially cND particles 'wet' the polymer phase, but polymers do not like to spread on the cND surface. On the other hand, the driving force for cND re-aggregation over time in the polymer phase is governed by $\Delta W_{DIS-AGG}$.

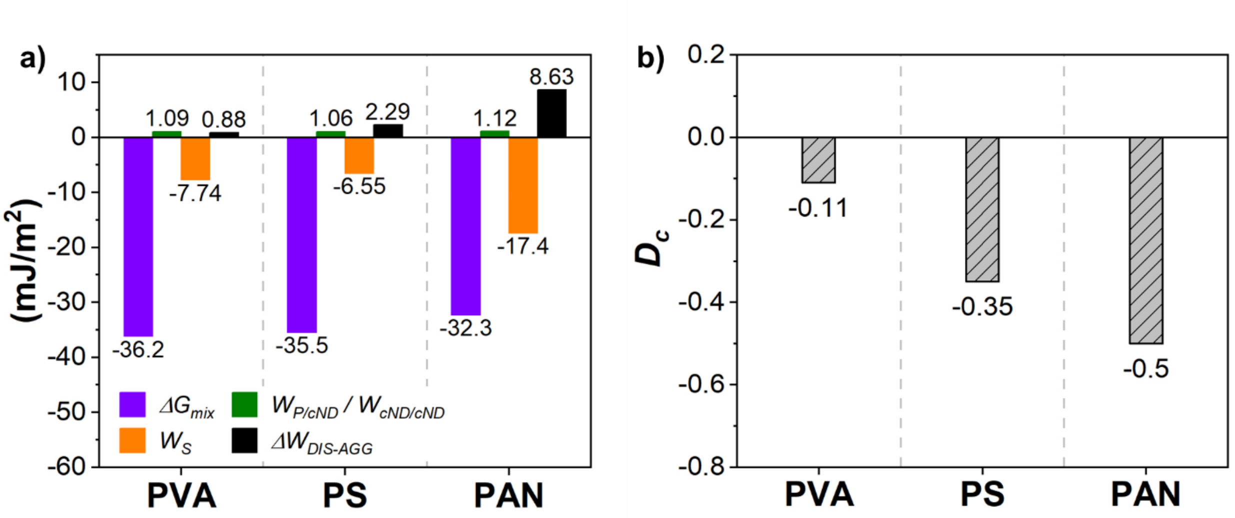

Figure 4. Thermodynamic parameters (a) free energy of mixing (ΔG_{mix}), wettability ratio ($W_{P/cND}/W_{cND/cND}$), work of spreading (W_S), work associated with dispersion-aggregation

transition ($\Delta W_{DIS-AGG}$), and (b) criterion for dispersion (D_c) derived for cND dispersion in two semi-crystalline polymers (PVA, PAN) and amorphous PS using surface energies.

Equation 12 implies that this driving force is more pronounced for systems that have disparate surface energies, i.e., higher tendency of re-aggregation under conditions of a larger mismatch in dispersive and polar surface energy components of polymer relative to the cND. To that end, cND aggregation driving force was found to be most pronounced in PAN due to the larger deviation in polar component of surface energies (Table 1) and the least in PVA (Figure 4a).

In the above discussion, however, there is no consistent correlation between wettability ratio, work of spreading and work associated with dispersion-aggregation transition. The simultaneous effect of all these mechanisms taking place from the initial dispersed state to the final aggregated state, therefore, can be captured using D_c, the criterion for dispersion. D_c values for PVA, PS and PAN are -0.11, -0.35 and -0.5 respectively, indicating the higher tendency of formation of stable polymer-cND composites in the order PAN<PS<PVA (Figure 4b). Here, the negative values of D_c impose limitations in polymer-cND interactions, suggesting that the system leans towards an aggregated state. This is particularly true for fillers without tailored surface functionalization. We now use the dispersion criterion to correlate the shifts in the glass transition temperature of the polymers, an experimental indicator of the polymer-filler interfacial interactions.

3.4 Glass Transition Temperature of cND-reinforced Polymer Fiber Composites

In the presence of nanofillers, the bulk polymer properties can change owing to both physical confinement of the polymer between the nanofiller particles as well as favorable polymer-filler interfacial interactions that aid in the reinforcement of mechanical, thermal, or electrical properties and thus improve polymer functionality. More specifically, polymer segmental mobility can be suppressed/enhanced in the presence attractive/repulsive polymer-filler interactions.[78-85] Nanofiller-induced perturbation in polymer mobility can be captured experimentally by measuring shifts in the glass transition temperature (T_g) of the composites. A negative shift in T_g corresponds to repulsive or weak interfacial interactions, leading to an increase in configurational entropy[80] as well as increased filler aggregation.[81] Attractive interactions, on the other hand, result in configurational constraints on the polymer mobility and enhance the T_g.[80] Cheng *et al.* demonstrated that polymer-nanofiller interfacial interactions can be controlled via size variation of the particles and by altering the surface functionality of the nanofillers. [81] Ramanathan *et al.* reported increments in T_g of over $40°C$ for PAN and □ $30°C$ for PMMA using functionalized graphene sheets with modulus and tensile strength showing similar trends.[82] Experiments by Chen *et al.* using PS-grafted gold nanoparticles in PS demonstrated both positive and negative shifts in T_g that were dependent on the grafting density and ratio of matrix to grafted polymer molecular weight.[83] Additional studies using graphene in PMMA matrix, which show enhancement in T_g[84] further corroborate the use of such measurements to evaluate the strength of polymer-filler interactions. This study, therefore, utilize the shifts in T_g of electrospun composite fibers measured using DSC to quantitatively infer the presence of attractive or repulsive interfacial interactions between polymer and cNDs. Reported values of T_g for polymers and their composites with cNDs represent inflection points extracted from DSC isotherms (Table 2).

The relative increase in the glass transition temperature of the composites over the pure polymer (ΔT_g) as a function of cND loading reveals the effect of polymer-cND interactions (Figure 5a). Pure PVA nanofibers exhibit T_g of $78.3 \pm 0.4°C$, close to reported values in the literature.[86] Incorporation of cND into PVA nanofibers causes a positive shift in T_g for all cND loadings up to 2 wt% used in this study. The shift in T_g increases with increase in cND loading with the largest shift at 1 wt% ($+4.3°C$) indicating that increasing amounts of cND hinder the segmental mobility of PVA chains. The multiple hydroxyl groups on the PVA backbone can participate in favorable hydrogen bonding with the surface carboxylic acid groups on cNDs, leading to strong interfacial interactions between PVA and cND that reduce polymer mobility and cause the observed positive shift in T_g. Indeed, work by Zhang *et al.* recently demonstrated positive shifts in T_g upon incorporation of SiO_2-exfoliated boron nitride nanoparticles in PVA films with the surface hydroxyl groups on SiO_2 forming hydrogen bonds with the hydroxyl groups on PVA.[85] Further increase in cND loading 2 wt%, however, shows no further increase in the shift. This saturation could be influenced by possible particle aggregation at 2 wt% in the semi-crystalline PVA, which favors cohesive cND-cND interactions, diminishing the likelihood of favorable interactions with the polymer.

Table 2. Glass transition temperature (T_g) of electrospun polymer fibers with varying cND loadings.

	T_g (°C) of polymer-cND electrospun fibers		
cND (wt.%)	**PVA**	**PS**	**PAN**
0	78.3 ± 0.4	103.6 ± 0.1	100.5 ± 0.1
0.1	79.5 ± 0.5	104.0 ± 0.1	100.7 ± 0.3
0.5	80.6 ± 0.6	104.3 ± 0.1	100.7 ± 0.1
1.0	82.6 ± 1.3	104.6 ± 0.2	101.6 ± 0.5
2.0	82.4 ± 1.1	105.6 ± 0.1	99.4 ± 0.2

Similar trends in ΔT_g are observed for PS composite fibers with increase in cND loading resulting in increased positive shifts in T_g. However, in contrast to PVA, the positive shifts did not saturate, and the maximum shift was obtained for 2 wt% sample ($+2°C$). This could be explained using the amorphous nature of micron-sized PS fibers compared to the semi-crystalline PVA nanofibers, where more particles could be accommodated without necessarily exerting an influence on the neighboring particles or hindering crystallinity. Another key observation is that compared to PVA, the magnitude of the positive shifts in T_g at each cND loading is lower with the shifts for 0.1 wt% ($+0.4°C$) and 0.5 *wt*% ($+0.7°C$) that could be well within standard errors of the instrument. The upper limit of c-ND loading (2 wt%) was capped to study reinforcement properties at low loadings only. The reported values suggest some influence of cND on the mobility of PS. The smaller positive shift in ΔT_g for PS (~2°C) compared to that of PVA (~4°C) could be a result of weaker *van der* Waals interactions at the PS-cND interface relative to much stronger hydrogen bonding between PVA and cND. In contrast to both PVA and PS, however, PAN composite fibers do not show positive shifts in T_g at cND loadings less than 1 wt% and a maximum shift of □$1°C$ at that loading. Further increase in cND loading results in a negative shift ($-1.1°C$) indicating unfavorable and repulsive interactions between PAN and cND. A possible explanation could be formation of cND aggregates at 2 wt% loading in PAN as was observed in SEM images. (Figure S8 and Figure S9).

The maximum observed positive shifts ($\Delta T_{g,\max}$) for the three polymer PVA, PS and PAN were plotted against the theoretically derived criterion of dispersion (D_c) based on the surface energetics of the polymer-cND system (Figure 5b). Clearly, the predictions of the tendency to form stable dispersion of cND in polymer (PAN<PS<PVA) through smaller values of D_c align well and linearly with the order of the maximum positive shifts (PAN<PS<PVA) suggesting a direct

correlation between adhesion parameters and ΔT_g. Thus, values of the criterion for dispersion can be useful to predict and compare the polymer-cND interfacial interactions.

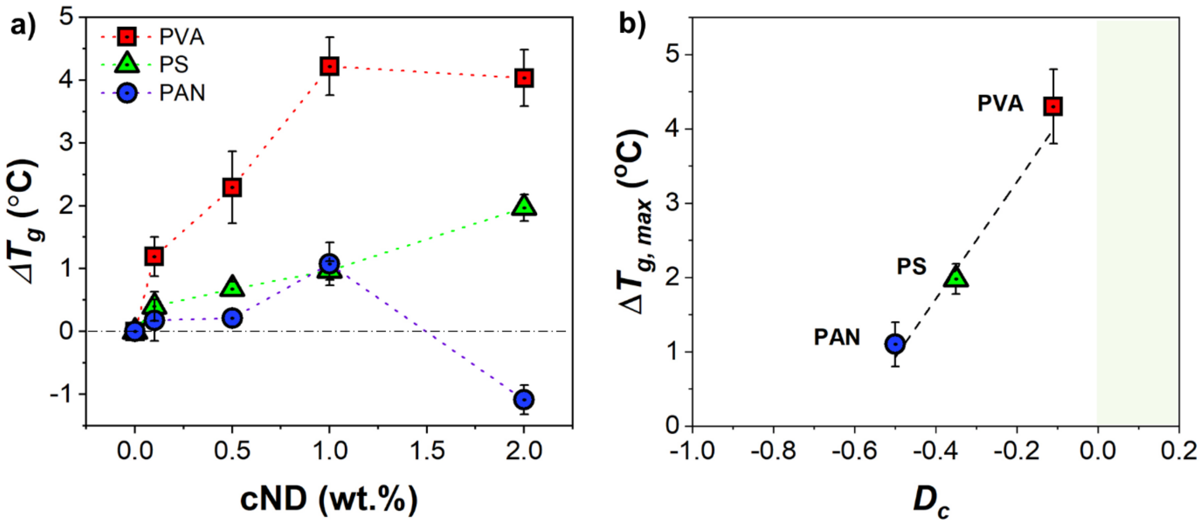

Figure 5. (a) Effect of cND addition on the relative shift in glass transition temperature (T_g) for PVA, PS and PAN electrospun nanofiber composites. (b) Linear correlation between the maximum shift in glass transition temperature ($\Delta T_{g,\max}$) and the criterion for dispersion (D_c). Small values of D_c (closer to 0) result in greater shifts in the order PAN<PS<PVA.

3.5 Correlation between T_g shifts, Tensile Strength and Polymer-cND Interfacial Interactions.

The agreement on the order of favorable interfacial interactions for the polymers-cND systems used in our study (PAN<PS<PVA) both from the theoretical criterion of dispersion values and the experimental maximum increments in glass transition temperature of the composites, prompted us to test whether the same holds true for the mechanical reinforcement potential of polymer-cND composites. Tensile strength (σ) and elongation at break (ε) as a function of cND loadings (Table 3) were obtained using stress-strain curves from a dynamic mechanical analyzer (Figure S7). PVA

nanofibers undergo elastic deformation for low strains (< 5%), and cND addition increases the stiffness of the polymer captured by the elastic modulus. After elastic deformation, the nanofibers start to yield and undergo further elongation, which results in fiber alignment, followed by fiber rupture (Figure S7a). Similar analysis is repeated for PAN and PS (Figures S7c and S7e). Stress-strain curves for PS with different cND loadings show initial elastic deformation in the low-strain region (<5%) similar to PVA but the fiber tensile strength in the range of 0.38-1.08 MPa is much lower than that of PVA ranging between 2.97-3.48 MPa. Much weaker PS-cND fibers, therefore, shows prolonged yielding since they are softer relative to PVA and does not yield immediately. The tensile strength of PAN-cND nanofibers (0.98-1.4 MPa) was intermediate between that of PS and PVA.

Table 3. Tensile strength (σ) and elongation at break (ε) of polymer nanofibers with different c-ND loadings obtained from stress-strain plots.

cND (wt.%)	**PVA**		**PS**		**PAN**	
	σ (MPa)	ε (%)	σ (MPa)	ε (%)	σ (MPa)	ε (%)
0	2.97 ± 0.10	126.2 ± 19.4	0.38 ± 0.13	10.4 ± 6.1	1.74 ± 0.07	18.9 ± 6.4
0.5	4.46 ± 0.42	99.3 ± 8.6	0.58 ± 0.12	18.0 ± 6.6	1.28 ± 0.29	13.9 ± 5.1
1.0	4.64 ± 0.08	77.1 ± 12.1	0.95 ± 0.35	17.3 ± 2.6	1.27 ± 0.20	9.42 ± 2.1
2.0	3.48 ± 0.13	44.8 ± 6.3	1.08 ± 0.13	19.7 ± 3.7	0.98 ± 0.18	9.37 ± 0.6

The normalized tensile strength of the polymer-cND composite fibers as a function of cND loading reveal close agreement with trends observed for the T_g shifts for PVA, PS and PAN (Figures 6a). Both PVA and PS fibers have higher tensile strengths while PAN fibers show reduction in tensile strength compared to the unmodified polymer base upon addition of cND. For

PVA, the tensile strength increases with increasing cND loading up to 1 wt% where the maximum reinforcement is observed (+56%) followed by a lowering of the positive shift (+17%) at 2 wt% loading, mimicking the trend observed in ΔT_g with a maximum shift also at 1 wt% (+4.3°C) followed by saturation of the PVA-cND interactions at 2 wt% possibly due to cND aggregation resulting in no further positive shifts (Figure 5a). Thus, the reinforcement potential for PVA-cND fibers aligns well with the strength of interfacial interactions predicted from glass transition temperature shifts. Despite the increase in tensile strength, increase in cND loadings reduces elongation at break for the composite fibers, with a maximum reduction of ~65% seen for 2 wt% loadings (Figure S7b). This could be a consequence of cND particles hindering the semi-crystalline structure of PVA. Indeed, the crystallinity of PVA, obtained using DSC, decreases with cND loadings (Figure S8). In sharp contrast to increase in tensile strength upon addition of cND in PVA, PAN shows no tensile strength reinforcement as seen by the normalized values of tensile strength, which are all less than unity for all cND loadings. At maximum loading of 2 wt%, PAN shows an approximate reduction of 44% in tensile strength, indicating negative effects of cND addition on reinforcement. Correlating this to shifts in T_g, we find that PAN did not interact well with cND and no significant enhancement was observed with a negative shift (-1.1°C) at 2 wt% further indicating that very weak or negligible interfacial interactions lead to no significant improvements in mechanical properties.

In the case of PS-cND composite fibers, the increase in tensile strength occurs at even low cND content and the trend does not reverse at higher loadings unlike that for PVA, again, similar to the trend observed for ΔT_g. Although the maximum ΔT_g for PS-cND was lower than that for PVA-cND (+1.97°C vs +4.3°C), the maximum enhancement in tensile strength was significantly higher for PS (56% vs 284%) such that the trend for maximum tensile reinforcement followed PAN<PVA<PS.

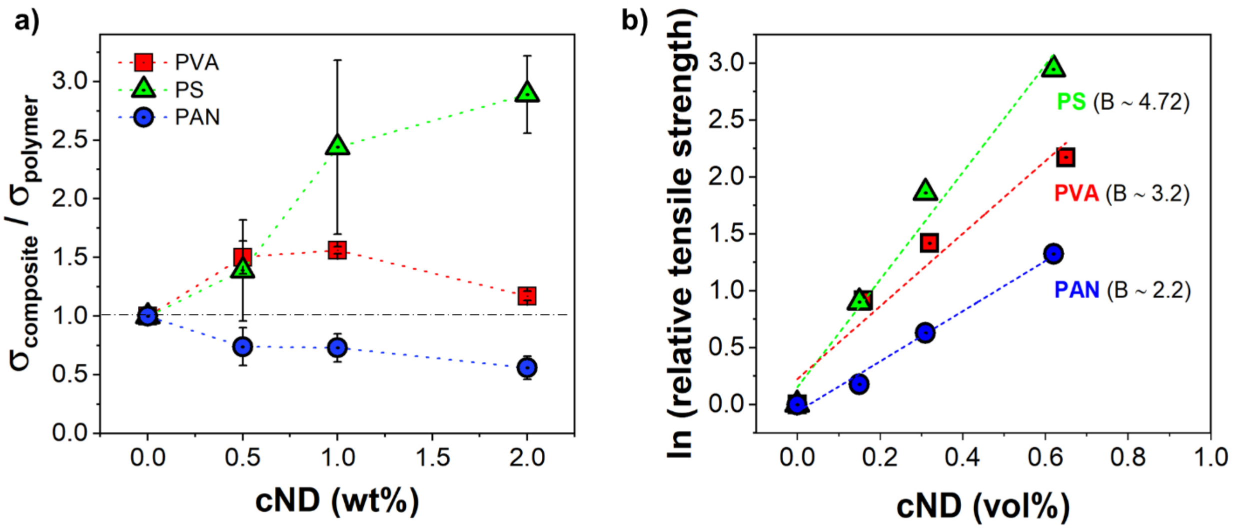

Figure 6. (a) Normalized tensile strength of polymer-cND composite fibers as a function of cND loading and (b) B parameter derived by fitting experimental tensile strength data as a function of cND loading (*vol*%) to Pukanszky model.

This is interestingly different from the predictions made by the criterion for dispersion and shifts in T_g which indicated the order of polymer-cND interfacial interactions to be PAN<PS<PVA. This means that apart from the adhesion parameters and interfacial interactions, other factors too may play a role in dictating mechanical reinforcement. Indeed, along with high polymer-filler interfacial strength, high stress transfer efficiency is also important for mechanical reinforcements in polymer-filler nanocomposites.[87-89] Several models in the literature, with assumptions from zero polymer-filler interfacial adhesion to very strong interfacial adhesion, have been used to predict the stress transfer efficiency of composite materials. In particular, an empirical model shown in eq

14, consisting of an interaction parameter (B) characterizing the interfacial interaction, thickness and strength of composites is used to fit the experimental data.

$$\ln\left[\frac{\sigma_c}{\sigma_p}\frac{1+2.5\phi_{cND}}{1-\phi_{cND}}\right]=B\phi_{cND} \tag{14}$$

In eq 14, σ_c is the tensile strength of the composite, σ_p is the tensile strength of the polymer, ϕ_F is the volume fraction of the cND and B is the capacity of stress transfer related to thickness and area of interface between the polymer and cND.[87,88] The first term physically represents a decrease in the effective cross-section by cND incorporation. Values of the B parameter are derived using the tensile strength data for the three polymer-cND systems (Figure 6b) and the important parameters related to cND reinforcement are summarized (Table 4).

Table 4. T_g shifts and normalized tensile strength as a function of cND loadings with Pukanszky B parameter (measure of stress transfer between polymer and cND) and theoretical criterion for dispersion obtained from surface energetics for cND-polymer systems.

cND	**PVA**			**PS**			**PAN**		
(wt.%)	$\Delta T_g (°C)$	σ_c / σ_p	(B, D$_c$)	$\Delta T_g (°C)$	σ_c / σ_p	(B, D$_c$)	$\Delta T_g (°C)$	σ_c / σ_p	(B, D$_c$)
0	0	1		0	1		0	1	
0.5	2.3 ± 0.6	1.50	3.20,	0.7 ± 0.1	1.52	4.72,	0.2 ± 0.3	0.74	2.2,
1.0	4.3 ± 0.5	1.56	-0.11	0.97 ± 0.2	2.50	-0.35	1.1 ± 0.1	0.73	-0.50
2.0	4.1± 0.5	1.17		1.98 ± 0.2	2.84		-1.1 ± 0.3	0.56	

The stress transfer efficiency as governed by the B parameter appears to increase in the order PAN<PVA<PS. Both the criterion of dispersion and the B parameter indicate that interfacial interactions are smallest and negligible for PAN compared to PVA and PS, a direct consequence

of the mismatch in surface energies that enhance the driving force for cND aggregation and reduce the interfacial area between polymer and cND, thereby reducing the stress transfer efficiency as well. For PS and PVA, the stress transfer driving force as indicated by B parameter is higher for PS while the resistance to aggregation as indicated by D_c is higher for PVA. This discrepancy may be a result of the different crystalline nature of the two polymers with PVA being semi-crystalline while PS is amorphous. The amorphous nature of PS fibers may provide more efficient stress transfer between PS-cND resulting in improved normalized tensile strength compared to PVA while the better interfacial interactions in semi-crystalline PVA-cND leading to higher positive shifts in T_g.

4. CONCLUSION

Development of nanocomposites with enhanced properties necessitates the use of model fillers as well as a fundamental understanding of polymer-filler interactions at the nanoscale. Nanodiamonds (NDs) have emerged as a novel class of nanofillers, however, the propensity of NDs to aggregate in solution as well as in polymers present significant challenges during processing of ND-based fibers composites. As such, understanding the interfacial energetics associated with polymer-ND composites to promote dispersion and enhance ND-polymer wetting at the nanoscale is an essential prerequisite in designing polymer-ND composite fibers with reinforced mechanical properties. In this work, we studied the aggregation behavior of carboxylated-ND (cND) in various solvents and polymers with varying polarities. Dispersion of cND in 18 different solvents revealed a dependence on the polar component of solvent solubility parameter, with stable to moderately stable dispersions observed in solvents with polar component of the solubility parameter higher than ~7 MPa$^{1/2}$. The cNDs ~100 nm in size were de-aggregated into smaller particles using salt-assisted ultrasonic de-aggregation resulting in cNDs with a primary particle size of ~20-30 nm. Wicking technique, combined with Washburn equation, was used to estimate surface energy of cND (33.5 ± 6.9 mJ/m^2).

cND between 20-30 nm were used to make electrospun fiber composites in two semi-crystalline polymers - PVA and PAN and amorphous PS. Thermodynamic parameters such as wettability, work of spreading, and work of dispersion-aggregation transition, calculated using the surface energy of cND and polymers, were used to derive a criterion for dispersion (D_c) as a predictor for interfacial interactions and final tensile properties of polymer-cND fiber composites. Shifts in glass transition temperature, used as a measure of polymer-cND interactions, showed a direct correlation with D_c in the order of PAN<PS<PVA. However, the final tensile strength showed a direct correlation with D_c and ΔT_g for semi-crystalline polymers only, with amorphous polystyrene showing maximum reinforcement contrary to predictions made by ΔT_g, suggesting contributions of crystallinity and stress transfer efficiency to final tensile strength. The correlations established in this study could pave way for tailoring the interface of polymer-NDs to ensure maximum interfacial interactions and corresponding mechanical reinforcement. The findings of this study could offer additional insights into the interface design for polymer-ND fiber composites.

ASSOCIATED CONTENT

The following file is available free of charge.

Hildebrand solubility parameters for solvent used in the cND dispersion study; additional characterization of as received cND dispersion stability and particle size in water over time and particle size reduction of SAUD cND prepared through microtip sonication via DLS measurements, conductometric titration curves for surface carboxylic acid content determination;

further information on electrospinning setup for polymer-cND composite fabrication; summary of all relevant adhesion parameters estimated for cND with PVA, PS and PAN polymers; stress-strain curves obtained from dynamic mechanical analyzer to determine tensile properties of electrospun composite fibers as a function of cND loading; morphology of fibers via SEM imaging and thermal stability of fibers evaluated using thermal gravimetry analysis (TGA) (PDF)

AUTHOR INFORMATION

Corresponding Author

*Saad A. Khan - Department of Chemical and Biomolecular Engineering, North Carolina State University, Raleigh, NC 27695, United States; Phone: 919-515-4519; Email: khan@eos.ncsu.edu

Authors

Prajesh Adhikari - Department of Chemical and Biomolecular Engineering, North Carolina State University, Raleigh, NC 27695, United States

Pallav K. Jani - Department of Chemical and Biomolecular Engineering, North Carolina State University, Raleigh, NC 27695, United States

Lilian C. Hsiao - Department of Chemical and Biomolecular Engineering, North Carolina State University, Raleigh, NC 27695, United States

Orlando J. Rojas - Bioproducts Institute, Departments of Chemical & Biological Engineering, Chemistry, and Wood Science, The University of British Columbia, Vancouver, BC V6T 1Z3, Canada; Department of Bioproducts and Biosystems, School of Chemical Engineering, Aalto University, FI-00076 Aalto, Espoo, Finland

Author Contributions

The manuscript was written through contributions of all authors. All authors have given approval to the final version of the manuscript.

Notes

The authors declare no competing financial interest.

ACKNOWLEDGMENT

The authors gratefully acknowledge The Nonwovens Institute (NWI) at North Carolina State University, Raleigh for supporting this study. This work was performed in part at the North Carolina State University Analytical Instrumentation Facility (AIF), which is supported by the State of North Carolina and the National Science Foundation (ECCS-2025064). The AIF is a member of the North Carolina Research Triangle Nanotechnology Network (RTNN), a site in the National Nanotechnology Coordinated Infrastructure (NNCI).

REFERENCES

1. Danilenko. On the history of the discovery of nanodiamond synthesis. *Phys. Solid State* **46**, 595–599 (2004).
2. Zhang *et al*. Nanodiamonds conjugated upconversion nanoparticles for bio-imaging and drug delivery. *J. Colloid Interface Sci.* **537**, 316-324 (2019).
3. Hsiao *et al.* Fluorescent Nanodiamond: A versatile tool for long-term cell tracking, super-resolution imaging, and nanoscale temperature sensing. *Acc. Chem. Res.* **49,** 400–407 (2016).
4. Hui *et al.* Nanodiamonds for optical bioimaging. *J. Phys. D. Appl. Phys.* **43,** 374021 (2010).
5. Chang *et al.* Mass production and dynamic imaging of fluorescent nanodiamonds. *Nat. Nanotechnol.* **3,** 284–288 (2008).
6. Long *et al.* "Two in one": Simultaneous functionalization and DOX loading for fabrication of nanodiamond-based pH responsive drug delivery system. *Mater. Sci. Eng. C* **108**, 110413 (2020).

7. Rehman, Houshyar and Wang, X. Nanodiamond in composite: Biomedical application. *J. Biomed. Mater. Res. A* **108**, 906-922 (2020).

8. Roy *et al.* Characterization of nanodiamond-based anti-HIV drug delivery to the brain. *Sci. Rep*. **8**, 1-12 (2018).

9. Mochalin *et al.* Adsorption of drugs on nanodiamond: toward development of a drug delivery platform. *Mol. Pharmaceutics* **10,** 3728-3735 (2013).

10. Zhang *et al.* Multimodal nanodiamond drug delivery carriers for selective targeting, imaging, and enhanced chemotherapeutic efficacy. *Adv. Mater.* **23**, 4770–4775 (2011).

11. Huang *et al*. Active nanodiamond hydrogels for chemotherapeutic delivery. *Nano Lett.* **7,** 3305–3314 (2007).

12. Cheng *et al*. Nanodiamonds suppress the growth of lithium dendrites. *Nature Commun.* **8**, 1-9 (2017).

13. Kausar, Ashraf, & Siddiq. Polymer/Nanodiamond composites in Li-Ion batteries: A Review. *Polym. Plast. Technol. Eng.* **53,** 550–563 (2014).

14. Kovalenko, Bucknall, and Yushin. Detonation nanodiamond and onion-like-carbon-embedded polyaniline for supercapacitors. *Adv. Funct. Mater.* **20,** 3979–3986 (2010).

15. Zang *et al*. Electrochemical properties of nanodiamond powder electrodes. *Diam. Relat. Mater.* **16,** 16–20 (2007).

16. Mirzaamiri *et al.* Molecular dynamics simulation and experimental investigation of tribological behavior of nanodiamonds in aqueous suspensions. *Tribol. Int.* **156**, 106838 (2021).

17. Shirani *et al.* Combined tribological and bactericidal effect of nanodiamonds as a potential lubricant for artificial joints. *ACS Appl. Mater. Interfaces* **11**, 43500-43508 (2019).

18. Ivanov & Shenderova. Nanodiamond-based nanolubricants for motor oils. *Curr. Opin. Solid State Mater. Sci.* **21,** 17–24 (2017).

19. Elomaa *et al.*. A comparison of tribological properties of evenly distributed and agglomerated diamond nanoparticles in lubricated high-load steel-steel contact. *Tribol. Int.* **71,** 62–68 (2014).

20. Sun *et al*. Enhancement in thermal conductivity of polymer composites through construction of graphene/nanodiamond bi-network thermal transfer paths. *Mater. Lett.* **271**, 127772 (2020).

21. Karami *et al*. Polymer/nanodiamond composites-a comprehensive review from synthesis and fabrication to properties and applications. *Adv. Colloid Interface Sci.* **269**, 122-151 (2019).

22. Houshyar *et al.* Nanodiamond/poly-ε-caprolactone nanofibrous scaffold for wound management. *Mater. Sci. Eng. C* **100**, 378-387 (2019).

23. Behler *et al.* Nanodiamond-polymer composite fibers and coatings. *ACS Nano* **3,** 363–369 (2009).

24. Dolmatov *et al*. Currently available methods of industrial nanodiamond synthesis. *Phys. Solid State* **46,** 611–615 (2004).

25. Shenderova *et al.* Surface chemistry and properties of ozone-purified detonation nanodiamonds. *J. Phys. Chem. C* **115,** 9827–9837 (2011).

26. Pichot *et al.* An efficient purification method for detonation nanodiamonds. *Diam. Relat. Mater.* **17,** 13–22 (2008).

27. Petrov *et al.* Detonation nanodiamonds simultaneously purified and modified by gas treatment. *Diam. Relat. Mater.* **16,** 2098–2103 (2007).

28. Osswald *et al*. Control of sp2/sp3 carbon ratio and surface chemistry of nanodiamond powders by selective oxidation in air. *J. Am. Chem. Soc.* **128,** 11635–11642 (2006).

29. Kulakova. Surface chemistry of nanodiamonds. *Phys. Solid State* **46,** 636–643 (2004).

30. Krueger and Boedeker. Deagglomeration and functionalisation of detonation nanodiamond with long alkyl chains. *Diam. Relat. Mater.* **17,** 1367–1370 (2008).

31. Krueger *et al.* Deagglomeration and functionalisation of detonation diamond. *Phys. Status Solidi Appl. Mater. Sci.* **204,** 2881–2887 (2007).

32. Mochalin *et al*. The properties and applications of nanodiamonds. *Nat. Nanotechnol.* **7,** 11–23 (2012).

33. Reina *et al.* Chemical functionalization of nanodiamonds: Opportunities and challenges ahead. *Angew. Chem. Int. Ed.* **58**, 17918 (2019).

34. Farias *et al.* Nanodiamond-stabilized pickering emulsions: Microstructure and rheology. *J. Colloid Interface Sci.* **580**, 180-191 (2020).

35. Xu *et a*. Influence of surface modification adopting thermal treatments on dispersion of detonation nanodiamond. *J. Solid State Chem.* **178,** 688–693 (2005).

36. Xu and Xue. A New Method for Deaggregation of nanodiamond from explosive detonation : Graphitization – Oxidation Method 1. *Phys. Solid State* **46,** 633–634 (2004).

37. Vul *et al.* Direct observation of isolated ultrananodimensional diamond clusters using atomic force microscopy. *Tech. Phys. Lett.* **32,** 561–563 (2006).

38. Osawa. Recent progress and perspectives in single-digit nanodiamond. *Diam. Relat. Mater.* **16,** 2018–2022 (2007).

39. Ozawa *et al.* Preparation and behavior of brownish, clear nanodiamond colloids. *Adv. Mater.* **19,** 1201–1206 (2007).

40. Liang, Ozawa & Krueger. A general procedure to functionalize agglomerating nanoparticles demonstrated on nanodiamond. *ACS Nano* **3,** 2288–2296 (2009).

41. Turcheniuk *et al*. Salt-Assisted Ultrasonic Deaggregation of Nanodiamond. *ACS Appl. Mater. Interfaces* **8,** 25461–25468 (2016).

42. Li *et al.* Improving thermal conductivity of poly (vinyl alcohol) composites by using functionalized nanodiamond. *Compos. Commun.* **23,** 100596 (2021).

43. Nan *et al.* Bioinspired modification strategy to improve thermal conductivity of flexible poly (vinyl alcohol)/nanodiamond nanocomposite films for thermal management applications. *Appl. Surf. Sci.* **508,** 144797 (2020).

44. Morimune *et al*. Poly(vinyl alcohol) nanocomposites with nanodiamond. *Macromolecules.* **44,** 4415–4421 (2011).

45. Kurkin *et al.* Structure of oriented fibers based on poly(vinyl alcohol) modified by detonation nanodiamonds. *Polym. Sci. - Ser. A* **50,** 43–50 (2008).

46. Jee and Lee. Mechanical properties of polycarbonate and poly(methyl methacrylate) films reinforced with surface-functionalized nanodiamonds. *J. Nanosci. Nanotechol*. **11,** 533-536 (2011).

47. Zhang *et al.* Mechanical properties and biomineralization of multifunctional nanodiamond-PLLA composites for bone tissue engineering. *Biomaterials* **33,** 5067–5075 (2012).

48. Branson *et al*. Fabrication and macro/nanoscale characterization of aggregated and highly de-aggregated nanodiamond/polyacrylonitrile composite thick films. *J. Mater. Chem.* **21,** 18832 (2011).

49. Roumeli *et al.* Factors controlling the enhanced mechanical and thermal properties of nanodiamond-reinforced cross-linked high density polyethylene. *J. Phys. Chem. B* **118,** 11341–52 (2014).

50. Sun *et al.* Enhancement in thermal conductivity of polymer composites through construction of graphene/nanodiamond bi-network thermal transfer paths. *Mater. Lett.* **271,** 127772 (2020).

51. Shvidchenko *et al.* Colloids of detonation nanodiamond particles for advanced applications. *Adv. Colloid Interface Sci.* **268,** 64-81 (2019).

52. Wang *et al.* Microscopic insight into nanodiamond polymer composites: reinforcement, structural, and interaction properties. *Nanoscale* **12,** 24107-24118 (2020).

53. Saito and Isogai. TEMPO-mediated oxidation of native cellulose. The effect of oxidation

conditions on chemical and crystal structures of the water-insoluble fractions. *Biomacromolecules* **5**, 1983–1989 (2004).

54. Owens and Wendt. Estimation of the surface free energy of polymers. *J. Appl. Polym. Sci.* **13,** 1741–1747 (1969).

55. Lander *et al*. A systematic comparison of contact angle methods. *Langmuir* **9,** 2237–2239 (1993).

56. Tretinnikov and Ikada. Dynamic wetting and contact angle hysteresis of polymer surfaces studied with the modified wilhelmy balance method. *Langmuir* **10,** 1606–1614 (1994).

57. Erbil *et al*. Determination of the receding contact angle of sessile drops on polymer surfaces by evaporation. *Langmuir* **15,** 7378–7385 (1999).

58. Bormashenko *et al.* Contact angle hysteresis on polymer substrates established with various experimental techniques, its interpretation, and quantitative characterization. *Langmuir* **24,** 4020–4025 (2008).

59. Chibowski and Holysz. Use of the Washburn equation for surface free energy determination. *Langmuir* **8,** 710–716 (1992).

60. Ji and Shi. A novel method for determining surface free energy of powders using Washburn's equation without calculating capillary factor and contact angle. *Powder Technol.* **271,** 88–92 (2015).

61. Paunov. Novel method for determining the three-phase contact angle of colloid particles adsorbed at air-water and oil-water interfaces. *Langmuir* **19,** 7970–7976 (2003).

62. Grimsey, Feeley and York. Analysis of the surface energy of pharmaceutical powders by inverse gas chromatography. *J. Pharm. Sci.* **91,** 571–583 (2002).

63. Fox *et al.* Simultaneously tailoring surface energies and thermal stabilities of cellulose nanocrystals using ion exchange: Effects on polymer composite properties for transportation, infrastructure, and renewable energy applications. *ACS Appl. Mater. Interfaces* **8,** 27270–27281 (2016).

64. Peng *et al*. Influence of drying method on the surface energy of cellulose nanofibrils determined by inverse gas chromatography. *J. Colloid Interface Sci.* **405,** 85–95 (2013)

65. Burns *et al*. Nanodiamond gels in nonpolar media: Colloidal and rheological properties. *J. Rheol.* **58,** 1599–1614 (2014).

66. Lim *et al*. Comprehensive evaluation of carboxylated nanodiamond as a topical drug delivery system. *Int. J. Nanomedicine*, **11**, 2381 (2016).

67. Fox, H. W. & Zisman, W. A. The spreading of liquids on low-energy surfaces. III. *Hydrocarbon Surfaces*. (1952).

68. Fowkes. Additivity of intermolecular forces at interfaces. I. Determination of the contribution to surface and interfacial tensions of dispersion forces in various liquids 1. *J. Phys. Chem.* **67**, 2538–2541 (1963).

69. Van Oss *et al*. Additive and nonadditive surface tension components and the interpretation of contact angles. *Langmuir* **4,** 884–891 (1988).

70. Neumann *et al*. An equation-of-state approach to determine surface tensions of low-energy solids from contact angles. *J. Colloid Interface Sci.* **49,** 291–304 (1974).

71. Spelt, Absolom and Neumann. Solid surface tension: The interpretation of contact angles by the equation of state approach and the theory of surface tension components. *Langmuir* **3,** 620–625 (1986).

72. Spelt and Neumann. Solid surface tension: the equation of state approach and the theory of surface tension components. Theoretical and conceptual considerations. *Langmuir* **3,** 588–591 (1987).

73. Graf and Riegler. Is there a general equation of state approach for interfacial tensions? *Langmuir* **16,** 5187–5191 (2000).

74. Lee. Scope and limitations of the equation of state approach for interfacial tensions. *Langmuir* **9,** 1898–1905 (1993).

75. Good and Girifalco. A theory for estimation of surface and interfacial energies. III. Estimation of surface energies of solids from contact angle data. *J. Phys. Chem*., **64**, 561-565 (1960).

76. Chibowski and Hołysz. On the use of Washburn's equation for contact angle determination. *J. Adhes. Sci. Technol.*, **11**, 1289-1301 (1997).

77. Stockelhuber *et al*. Contribution of physico-chemical properties of interfaces on dispersibility, adhesion and flocculation of filler particles in rubber. *Polymer (Guildf).* **51,** 1954–1963 (2010).

78. Natarajan *et al*. Effect of interfacial energetics on dispersion and glass transition temperature in polymer nanocomposites. *Macromolecules* **46,** 2833–2841 (2013).

79. Wang. Effect of polymer-filler and filler-filler interactions on dynamic properties of filled vulcanizates. *Rubber Chem. Technol.* **71**, 520-589 (1998).

80. Roldughin *et al*. Effect of hybrid nanoparticles on glass transition temperature of polymer nanocomposites. *Polymer Composites*, **37**, 1978-1990 (2016).

81. Cheng *et al*. Big effect of small nanoparticles: a shift in paradigm for polymer nanocomposites. *ACS nano*, **11**, 752-759 (2017).

82. Ramanathan *et al*. Functionalized graphene sheets for polymer nanocomposites. *Nat.*

Nanotechnol. **3,** 327–331 (2008).

83. Chen *et al.* Glass transition temperature of polymer-nanoparticle composites: Effect of polymer-particle interfacial energy. *Macromolecules* **46,** 4663–4669 (2013).

84. Liao *et al*. Does graphene change T_g of nanocomposites? *Macromolecules* **47,** 8311–8319 (2014).

85. Zhang *et al*. Large improvement of thermal transport and mechanical performance of polyvinyl alcohol composites based on interface enhanced by SiO_2 nanoparticle-modified-hexagonal boron nitride. *Compos. Sci. Technol.* **169**, 167-175 (2019).

86. Mahendia *et al*. Determination of glass transition temperature of reduced graphene oxide-poly (vinyl alcohol) composites using temperature dependent Fourier transform infrared spectroscopy. *J. Mol. Struct.* **1111**, 46-54 (2016).

87. Lazzeri and Phuong. Dependence of the Pukánszky's interaction parameter B on the interface shear strength (IFSS) of nanofiller- and short fiber-reinforced polymer composites. *Compos. Sci. Technol.* **93,** 106–113 (2014).

88. Zare. 'a' interfacial parameter in Nicolais-Narkis model for yield strength of polymer particulate nanocomposites as a function of material and interphase properties. *J. Colloid Interface Sci.* **470,** 245–249 (2016).

89. Li, Zare and Rhee. The percolation threshold for tensile strength of polymer/CNT nanocomposites assuming filler network and interphase regions. *Mater. Chem. Phys.* **207**, 76-83 (2018).